Pingfan Hu[1]
Artie McFerrin Department of Chemical Engineering,
Texas A&M University,
College Station, TX 77843

Changjie Cai[1]
The University of Oklahoma Health Sciences Center,
Oklahoma City, OK 73126

Hang Yi[1]
School of Chemical Engineering,
Oklahoma State University,
Stillwater, OK 74078

Jianan Zhao
School of Chemical Engineering,
Oklahoma State University,
Stillwater, OK 74078

Yu Feng[2]
School of Chemical Engineering,
Oklahoma State University,
420 Engineering North,
Stillwater, OK 74078
e-mail: yu.feng@okstate.edu

Qingsheng Wang[2]
Artie McFerrin Department of Chemical Engineering,
Texas A&M University,
College Station, TX 77843
e-mail: qwang@tamu.edu

Aiding Airway Obstruction Diagnosis With Computational Fluid Dynamics and Convolutional Neural Network: A New Perspective and Numerical Case Study

It is challenging to locate small-airway obstructions induced by chronic obstructive pulmonary disease (COPD) directly from visualization using available medical imaging techniques. Accordingly, this study proposes an innovative and noninvasive diagnostic method to detect obstruction locations using computational fluid dynamics (CFD) and convolutional neural network (CNN). Specifically, expiratory airflow velocity contours were obtained from CFD simulations in a subject-specific 3D tracheobronchial tree. One case representing normal airways and 990 cases associated with different obstruction sites were investigated using CFD. The expiratory airflow velocity contours at a selected cross section in the trachea were labeled and stored as the database for training and testing two CNN models, i.e., ResNet50 and YOLOv4. Gradient-weighted class activation mapping (Grad-CAM) and the Pearson correlation coefficient were employed and calculated to classify small-airway obstruction locations and pulmonary airflow pattern shifts and highlight the highly correlated regions in the contours for locating the obstruction sites. Results indicate that the airflow velocity pattern shifts are difficult to directly visualize based on the comparisons of CFD velocity contours. CNN results show strong relevance exists between the locations of the obstruction and the expiratory airflow velocity contours. The two CNN-based models are both capable of classifying the left lung, right lung, and both lungs obstructions well using the CFD simulated airflow contour images with total accuracy higher than 95.07%. The two automatic classification algorithms are highly transformative to clinical practice for early diagnosis of obstruction locations in the lung using the expiratory airflow velocity distributions, which could be imaged using hyperpolarized magnetic resonance imaging. [DOI: 10.1115/1.4053651]

Keywords: noninvasive airway obstruction diagnosis, computational fluid dynamics (CFD), convolutional neural network (CNN), gradient-weighted class activation mapping (Grad-CAM), ResNet50, YOLOv4 (Darknet53)

1 Introduction

According to the National Vital Statistics Report [1], chronic obstructive pulmonary disease (COPD) is the third leading cause of death in America. COPD causes severe breathing difficulty due to airway stiffening, loss of airway deformation capability, and airway blockage induced by inflammation, especially in small airways, which are regarded as the silent zone in the respiratory system [2–4]. Inhalation of therapeutic nano-/microparticles is one of the standard COPD treatments. However, the long-standing barrier of the pulmonary drug administration via inhalation therapy has been the inability to deliver a sufficiently high dose of therapeutic nano-/microparticles to obstruction sites in small airways to further improve the drug bio-availability and achieve desired therapeutic outcomes [3].

To overcome such a barrier, it is important to first detect the obstruction locations in small airways of COPD patients at an early stage and optimize the inhalation therapy to achieve targeted drug delivery to designated obstruction sites, instead of healthy airway tissues, for better therapeutic outcomes and reduced side effects. However, there is strong evidence to suggest that most patients are not aware of their small airway obstruction conditions at the early stage, due in part to the invasive nature of conventional diagnostic methods [5–7]. Specifically, traditional methods to diagnose pulmonary diseases involve costly and invasive procedures such as X-ray screening and bronchoscope. Thus, it is imperative and beneficial to detect the obstruction locations in peripheral lung precisely with noninvasive diagnostic methods.

To pave the way to a noninvasive and automatic diagnostic method based on additional clinically measurable human data, i.e., intrathoracic expiratory airflow velocity distributions [8–11], this study proposes and tests the feasibility of a new diagnostic methodology using both computational fluid dynamics (CFD) and convolutional neural networks (CNN), i.e., "the expiratory airflow pattern analysis," to identify the obstruction location in left or right lung deeper than generation 6 (G6) by automatic detection of the clinically measurable intrathoracic airflow pattern shifts using hyperpolarized magnetic resonance imaging (MRI) [8–11].

---

[1] Pingfan Hu, Changjie Cai, and Hang Yi authors contributed equally to this paper.

[2] Corresponding authors.

Contributed by the Fluids Engineering Division of ASME for publication in the JOURNAL OF FLUIDS ENGINEERING. Manuscript received October 29, 2021; final manuscript received January 18, 2022; published online March 8, 2022. Assoc. Editor: Arindam Banerjee.

Such a method was driven by a central hypothesis enlightened by existing preliminary studies [12], i.e., the small airway obstruction will lead to detectable velocity distribution pattern shift of the expiratory airflow in the trachea. Specifically, based on the training and test data generated using the CFD simulation results of expiratory airflows in a subject-specific human tracheobronchial tree (trachea to G6), two CNN-based classification models were developed using open-source codes ResNet50 [13] and YOLOv4 (Darknet53) [14]. The modified ResNet50 model is a 50-layer residual network, and it was the winner of the ImageNet large scale visual recognition challenge in 2015. The main goal of the residual network is to build a deeper neural network without the problem of vanishing gradients. To further analyze which regions suggest the obstruction locations, gradient-weighted class activation mapping (Grad-CAM) was applied to produce a coarse localization map highlighting the important regions [15]. The results were also validated by Darknet53 that acts as a backbone for the YOLOv4 object detection approach [16–19].

Although several diagnostic methods, i.e., computed tomography images-based measurements, respiratory acoustics-based approaches, spirometry, and forced oscillation techniques, have been applied on lung disease detection combined with machine learning [20–24], they did not attempt to achieve local or regional obstruction detection. To the best of our knowledge, the only two existing efforts in combining machine learning and computational lung aerosol dynamics method for lung disease diagnosis were made by Xi et al. [25,26], focusing on categorizing exhaled aerosol patterns that were simulated by CFD with different asthma conditions using fractal analysis and support vector machines (SVMs) classification as well as random forest. Therefore, this study is the first to develop two CNN-based classification models to automatically detect and locate airway obstructions in small airways based on airflow velocity distributions in the trachea. As the prototype of the noninvasive diagnostic method, CNN algorithms have the potential to be extended to locate small airway obstructions that may not be detectable *via* existing pulmonary health tests. By continuously extending the CNN training with additional subject-specific human respiratory configurations and airflow patterns, physicians only need to input the medical image of the airflow velocity contour at the predetermined cross section in the trachea measured by hyperpolarized MRI, and the obstruction locations will be automatically detected.

Accordingly, the objective of this study is to address the current diagnosing deficiency, i.e., the incapability to identify the obstruction locations in left or right lungs, by proposing and testing the feasibility of an innovative noninvasive diagnostic method to assist in the detection of obstruction locations in the peripheral lung using CFD and CNN methods. Two CNN-based models, i.e., modified ResNet50 and YOLOv4, are trained by CFD expiratory velocity contours in a subject-specific 3D tracheobronchial (TB) tree with 990 obstruction conditions at small airway terminals to automatically classify COPD airway obstruction locations. Grad-CAM and hue-value-saturation (HSV) thresholding techniques were employed to classify COPD obstruction locations and velocity contour pattern shifts in the lung and highlight the highly correlated regions in the contours for locating the obstruction sites. Velocity contours and Pearson correlation coefficients between (1) different obstruction locations and (2) true and false positive cases were also compared to analyze the significance of airflow pattern shifts. Specifically, false positive indicates that obstruction locations diagnosed by the CNN-based models are not correct.

2 Method

2.1 Study Design. Based on the central hypothesis, the workflow of the training and test of the two CNN classification models are shown in Figs. 1(*a*) and 1(*b*). A subject-specific TB tree from the trachea to G6 was employed for the expiratory flow simulations using CFD. An experimentally validated CFD model [27] was employed to predict expiratory intrathoracic flow velocity distributions through the TB tree with 990 airway obstruction conditions. Using the airflow velocity distribution data labeled by the obstruction locations, two CNN-based classification models were trained and tested.

2.2 Expiratory Flow Simulations Using Computational Fluid Dynamics

2.2.1 Airway Geometry and Mesh. As the first effort to test the feasibility of using CNN-based models to detect small airway obstruction locations, only one subject-specific TB tree geometry was employed in this in silico case study. Specifically, the geometry covers from the trachea to G6 (see Fig. 2). The TB tree contains 44 small airway openings in total. Polyhedral mesh with prism layers was used for mesh generations. The final mesh determined by the mesh independence test contains 1,255,200 elements and 3,853,278 nodes. CFD models [27,28] have been employed to simulate the expiratory flow patterns with a fixed total expiratory flow rate at the mouth (i.e., 60 L/min) and different obstruction sites at the 44 small airway terminals, preparing the training and test image database. Case statistics of obstruction locations of all cases are summarized in Fig. 3.

2.2.2 Governing Equations. The airflow dynamics of the respiratory tract are always unsteady and driven by the pressure differences under the action of the cyclic breathing process. In this study, the expiratory flow rate is assumed to be constant with a total expiratory flow rate $Q_{\text{in}} = 60\,\text{L/min}$, consistently for all obstruction conditions. The conservation laws of mass and momentum that solved can be written in tensor form, i.e.,

$$\frac{\partial u_i}{\partial x_i} = 0 \tag{1}$$

$$\rho\frac{\partial u_i}{\partial t} + \rho\frac{\partial(u_j u_i)}{\partial x_j} = -\frac{\partial p}{\partial x_i} + \frac{\partial}{\partial x_j}\left[(\mu+\mu_t)\left(\frac{\partial u_i}{\partial x_j}+\frac{\partial u_j}{\partial x_i}\right)\right] + \rho g_i \tag{2}$$

where u_j represents the airflow velocity, p is the pressure, g_j is the gravity, and μ_t is the turbulent viscosity. With $Q_{\text{in}} = 60\,\text{L/min}$, the expiratory airflow regime in the TB tree is laminar-to-turbulence transitional flow. Therefore, the transition shear stress transport (SST) model [29] was adapted for this study, predicting "laminar-to-turbulent" transition onset and providing a better balance between computational efficiency and accuracy when compared to large eddy simulations proved in the open literature [30,31].

2.2.3 Boundary Conditions. The 44 small G6 airway terminal openings (see Fig. 2) were assigned as velocity inlets. With the 1 or 2 designated obstructions in G6 airway openings from case to case, the total inlet area was slightly changed, and the inlet airflow velocities were also changed accordingly to match the condition that the total expiratory flow rate $Q_{\text{in}} = 60\,\text{L/min}$. The trachea opening (see Fig. 2) was assigned as the pressure outlet with zero gauge pressure. Airway walls were assumed to be static and nonslip.

2.2.4 Computational Fluid Dynamics Model Validations. The accuracy of the transition SST model has been experimentally validated by previous studies [27,28]. The use of the transition SST model was also validated with 3D velocity distributions in a physical model of a subject-specific human respiratory system measured experimentally [30]. Therefore, it can be justified that the pulmonary airflow simulated by the CFD model can represent the flow characteristics in human respiratory systems.

2.2.5 Training and Testing Database Preparation. As shown in Figs. 1(*a*) and 1(*b*), the preparation of the training and test database used the CFD simulation results for the expiratory flow field predictions with different obstruction conditions in the subject-

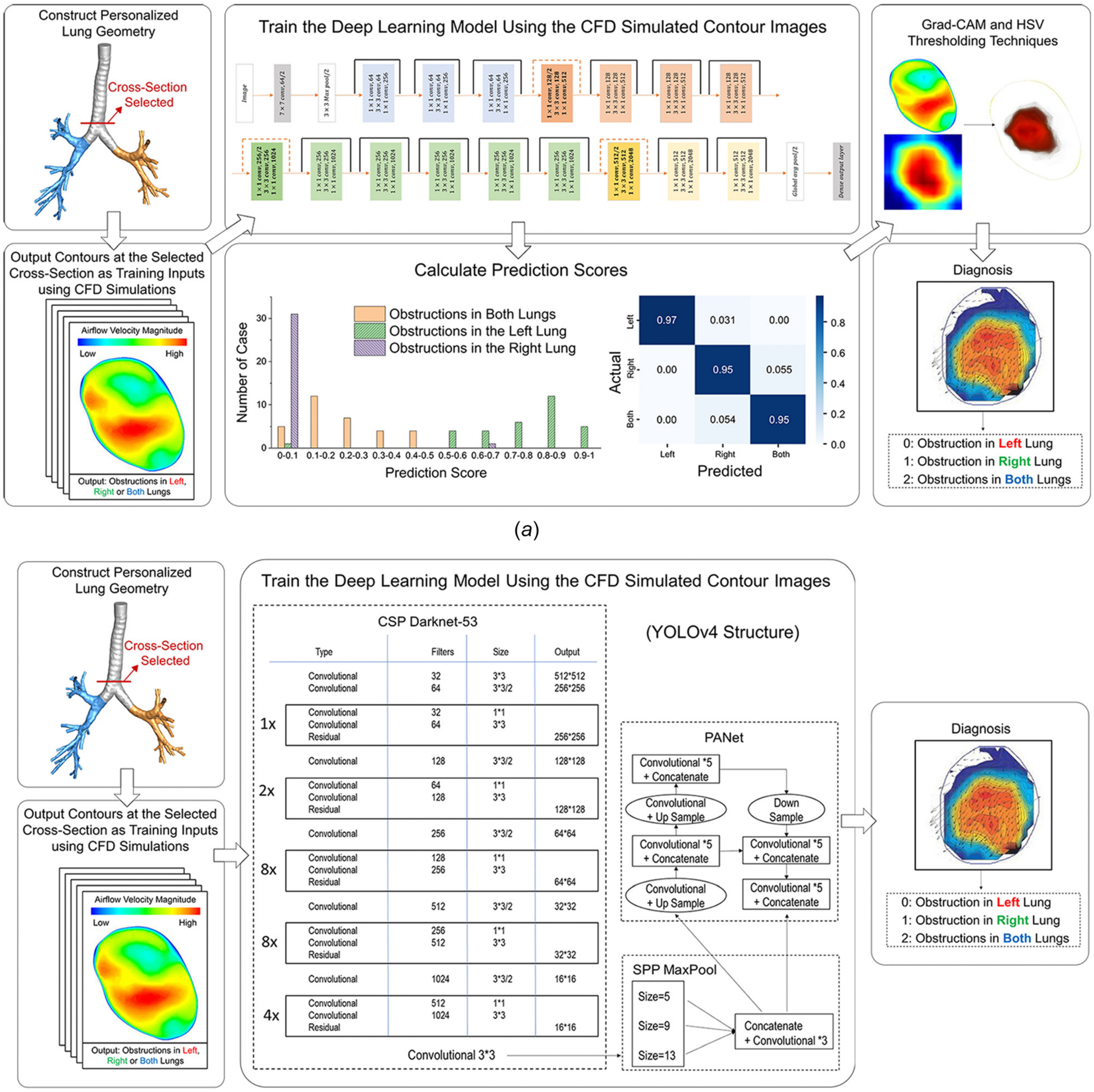

(*a*)

(*b*)

Fig. 1 Workflows of CNN development to diagnose obstructed locations in the human lung based on expiratory flow patterns: (*a*) ResNet50 and (*b*) YOLOv4 (Darknet53)

specific TB tree (see Fig. 2). Specifically, only 1 or 2 of the 44 small airway openings were blocked for each simulation case in order to mimic the minimum changes in obstruction conditions in the human lung compared with the obstructions of multiple openings in left, right, or both lungs. The structure of the labeled training and test images is shown in Fig. 3.

The velocity contours used for training and testing the two CNN-based models were acquired at a selected cross section ($x = 0.1$ m) for all CFD simulation cases. The cross section was selected based on two rationales, i.e., (1) the available locations in the chest where the airflow velocity distributions can be measured by hyperpolarized MRI, and (2) the location that is closer to the obstruction sites at 44 small airway terminals. Specifically, the closer the selected cross section and the obstruction sites are, the more negligible the dissipation effect will be, and the more identifiable shifts of the airflow velocity distributions can be maintained due to the variation in deeper lung expiratory flow conditions induced by the obstruction. An example of the expiratory velocity contour at $x = 0.1$ m can be found in Figs. 1(*a*) and 1(*b*). All contours were stored in Microsoft Windows Bitmap Format (BMP) format as the training and test database. The BMP images labeled by the obstruction sites can be found in Supplemental Material S1 on the ASME Digital Collection. The images were partitioned into training and testing sets for each obstruction class, with an approximately 80% to 20% split and five-fold cross-validation.

2.3 Obstruction Classification Using Two Convolutional Neural Network-Based Models. Convolutional neural network has been applied successfully in many areas, especially in object detection [32–35]. In this study, two open-source CNN algorithms, i.e., ResNet50 and YOLOv4 (Darknet53), were employed

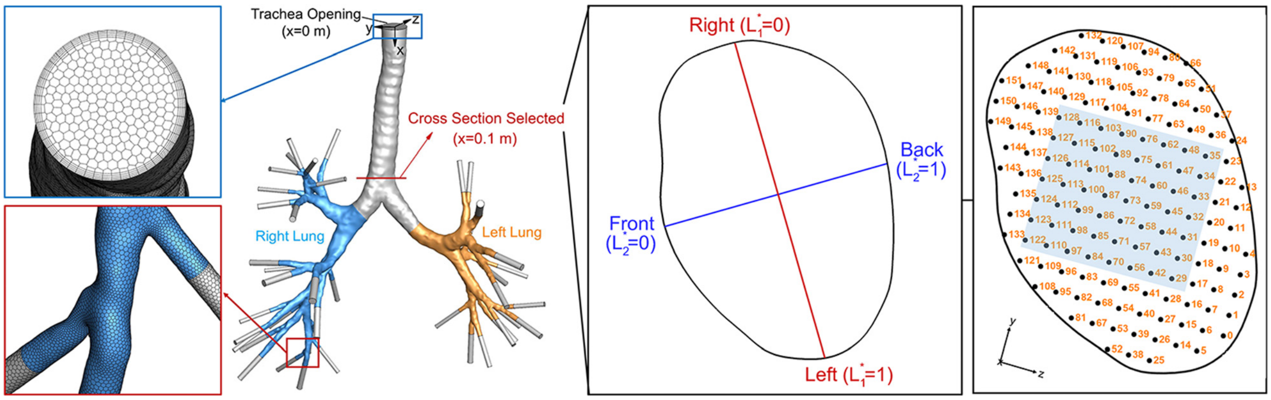

Fig. 2 Geometry and mesh details of the subject-specific human TB tree

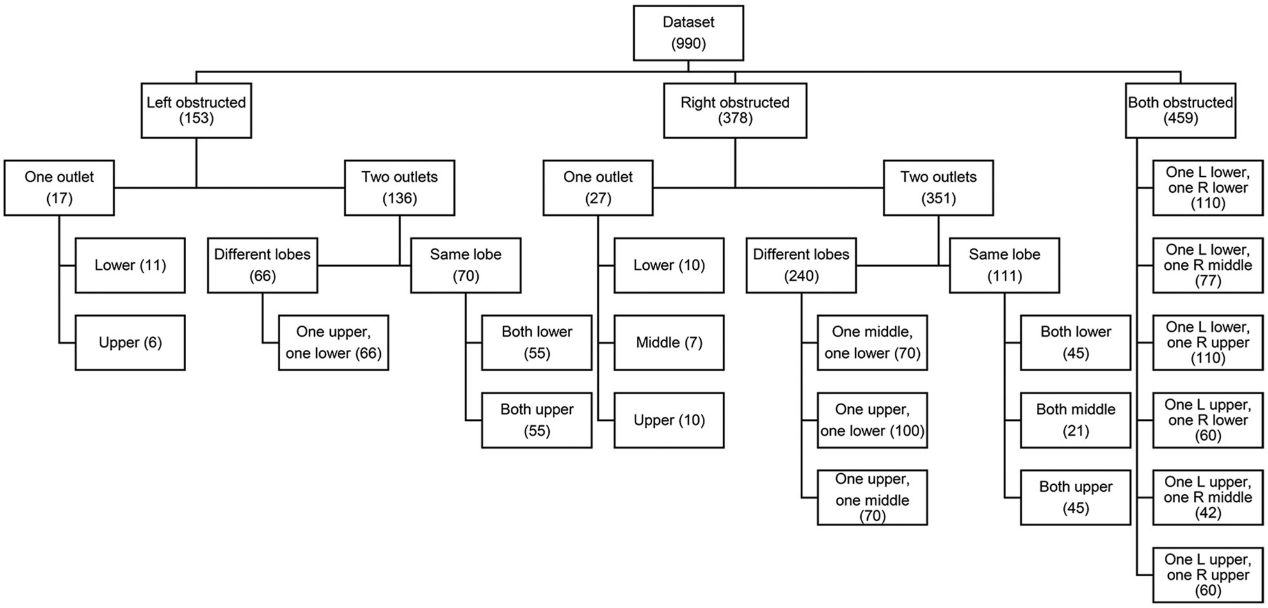

Fig. 3 Data structure of the training and test images prepared using CFD

to recognize the lung obstruction locations, including left lung, right lung, and both lungs.

2.3.1 Resnet50. As shown in Fig. 1(*a*), ResNet50 is a 50-layer residual network. The main goal is to build a deeper neural network based on a modified ResNet50 without encountering the vanishing gradient problem [36]. The error gradients are computed at the end of the network. Backpropagation [37] is used to propagate the error gradients backward through the network. Using the chain rule [37], multiplying terms with the error gradients have to be kept as the networks go backward. However, in the long chain of multiplication, the gradient becomes very small as networks approach the earlier layers in a deep architecture. This small gradient is an issue because network parameters cannot be updated by a large enough amount and the training is very slow. To avoid the vanishing gradient problem, ResNet50 stacks these residual blocks together where an identity function is used to preserve the gradient. It is also called skip connection since the origin input is added to the output of the convolution block directly. The structure of the skip connection is shown in Fig. 4 [13].

As shown in Figs. 1(*a*) and 5, the input image goes through the first layer with 64 filters with a filter size of 7 × 7. Next, it goes through the max pooling layer, which helps reduce the spatial size of the convolved features and also helps reduce the over-fitting problem. Then, it goes through 48 convolutional layers with skip connection, and finally reaches the fully connected layer that helps learn nonlinear combinations of the high-level features outputted by previous layers. In the modified ResNet50 model employed in

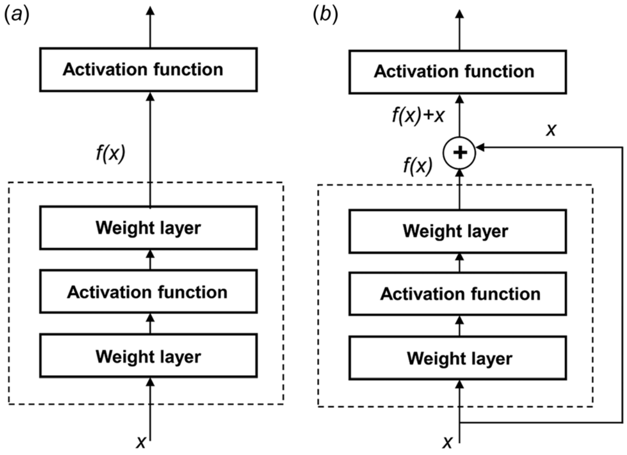

Fig. 4 The residual learning building blocks: (*a*) regular block and (*b*) residual block

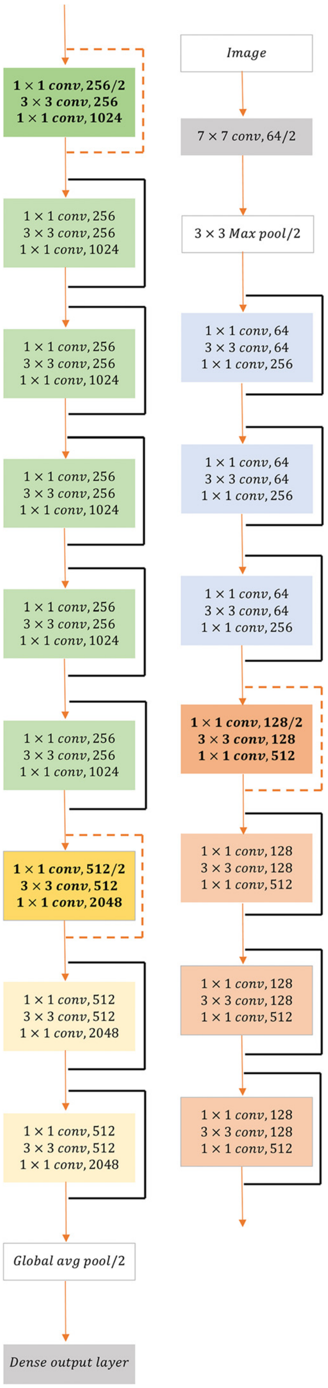

Fig. 5 Modified ResNet50 architecture

this study, parameters of the pretrained convolutional layers on the IMAGENET dataset [38] were used. The final pooling and fully connected layer in the original ResNet50 model were replaced by global average pooling and a dense output layer to connect the dimensions of the previous layers with the new layers for making classification for our own dataset. Regularization methods (i.e., Batch normalization and dropout) and optimizers were used to avoid overfitting and reduce computational time [13].

2.3.2 Yolov4 (Darknet53). One popular state-of-the-art CNN-based model for detecting objects in an image is "You Only Look Once" or YOLO [39]. YOLO version 3 (v3) expands on its previous version, i.e., YOLOv2, by utilizing a Darknet53 (53 convolutional layers) as its backbone in contrast to YOLOv2, which utilized Darknet19 (19 convolutional layers) [40,41]. Although the precision has been greatly improved in YOLOv3 compared with YOLOv2 due to the more convolutional layers, the resultantly increased computational complexity also makes YOLOv3 computationally more expensive. To optimize the balance between precision and computational efficiency, YOLOv4 has been developed to improve both the precision and speed of YOLOv3. YOLOv4 is considered one of the most accurate real-time neural network detectors to date [14]. YOLOv4 has been successfully applied in various industries, including autonomous driving, agriculture, electronics, and public health [16–19]. In this study, YOLOv4 of recognizing was employed and tested for classifying the lung obstruction locations, including left lung, right lung, and both lungs.

As shown in Fig. 1(*b*), YOLOv4 consists of three main blocks, including the "backbone", "neck", and "head" [14]. The "backbone" acts as feature extraction. The model implements the cross stage partial network (CSPNet) backbone method to extract features [42], containing 53 convolutional layers for accurate image classification, also known as CSPDarknet53. The "neck" is a layer between the "backbone" and "head," acting as feature aggregation. Specifically, YOLOv4 uses the path aggregation network (PANet) for feature aggregation [43] and spatial pyramid pooling method to set apart the important features obtained from the "backbone" [43]. The "head" used in YOLOv4 is the same as the one in YOLOv3, which uses dense prediction for anchor-based detection that helps divide the image into multiple cells and inspect each cell to find the probability of having an object using the postprocessing techniques [41].

It has been shown that, with a clean (clean annotations) set of full-resolution images, object recognition can be more accurate, especially by exploiting more feature-level information [38]. Therefore, high-resolution velocity-contour figures (2048 pixels × 1536 pixels) were acquired from CFD simulation results and labeled as the training and test database (see Fig. 3). A total of 990 images, i.e., the expiratory airflow velocity contour at the selected cross section ($x = 0.1$ m), were generated from the CFD modeling, including 153 of left lung obstructions, 378 of right lung obstructions, and 459 of both lung obstructions. All images were annotated utilizing Yolo_mark, which allows for objects to be marked within the images. The program was compiled in Microsoft Visual Studio 2019 to run on windows operating system with OpenCV. A text file was created with a list of the names (or classes) and locations (X- and Y-coordinates, and height and width of the bounding box) of each class. The annotated images were then used for training the YOLOv4 model for detection.

2.4 Gradient-Weighted Class Activation Mapping.

In practice, deep learning models are treated as "black box" methods. To enhance the fundamental understanding of where the CNN-based models are "looking" in the input image, a simple modification of the global average pooling layer combined with Grad-CAM [44] allows the classification-trained CNN to both classify the image and localize class-specific image regions. The gradient of the chosen convolutional layer is converted to weight. Then the 1D vector that stored the number of filters is reshaped to the image shape. After the layer output and weight are computed and normalized, the heat map showing the highly correlated regions of input for predictions is created. By generating such visual explanations, Grad-CAM makes the CNN-based model more transparent and insightful.

3 Numerical Setup

To obtain the expiratory airflow fields with different obstruction locations, CFD simulations were performed using ANSYS FLUENT 2021 R1 on a local 64-bit Dell 7910 workstation (dual processors, 32 cores 3.1 GHz, and 256GB RAM) and the supercomputers in the High Performance Computing Center at Oklahoma State University (e.g., Cowboy cluster machine with 252 standards compute

Table 1 Evaluation metrics of modified Resnet50 and YOLOv4 models

Evaluation metrics	ResNet50 test[a]	YOLOv4 test 01[b]	YOLOv4 test 02[c]
Macro-precision $P = \mathrm{TP}/(\mathrm{TP}+\mathrm{FP})$	93.86%	93.00%	96.00%
Macro-recall $R = \mathrm{TP}/(\mathrm{TP}+\mathrm{FN})$	95.27%	94.00%	97.00%
F1 score $F1 = 2P \cdot R/(P+R)$	94.56%	93.00%	96.00%
AP (left lung obstructed)	89.27%	100%	100%
AP (right lung obstructed)	93.89%	96.78%	97.74%
AP (both lungs obstructed)	98.42%	93.85%	96.29%

[a] Resnet50 Test: 153 images for left, 378 images for right, and 459 images for both lung obstructions.
[b] YOLO Test 01: 153 images for left, 153 images for right, and 153 images for both lung obstructions.
[c] YOLO Test 02: 153 images for left, 378 images for right, and 459 images for both lung obstructions.
TP = true positive, FP = false positive, FN = false negative.

nodes with dual Intel Xeon E5-2620 “Sandy Bridge” hex core 2.0 GHz CPUs, with 32 GB of 1333 MHz RAM). All variables, including velocity components, pressure, and turbulence variables, are located at the centroids of the discretized mesh cells. An improved Rhie–Chow interpolation method [45] was employed to obtain the velocity components, pressure, and turbulence on the control volume faces from those at the control volume centers. A quadratic upwind differencing scheme, which is third-order accurate in space, will be used to model the advective terms of the transport equations. The typical single-CPU time to complete one simulation is approximately 1.3 h. The modified ResNet50 model was coded and compiled in KERAS 2.4.3. It was run on windows operating system with graphic processing unit GeForce RTX 2080 with 16 GB-VRAM. The training computation is approximately 12 s per epoch with 19 min and 10 s in total. The YOLOv4-based CNN model was compiled in Microsoft Visual Studio 2019 (Microsoft Corporation, Albuquerque, NM) and run on windows operating system with graphic processing unit (GeForce GTX 1660 Ti with 16 GB-VRAM), CUDNN_HALF, and OpenCV for accelerating the training. For Test 2 shown in Table 1, the training computation is approximately 10 s per iteration with batch size of 64, subdivisions (or mini batch-size) of 64, and 6000 iterations in total; therefore, the training computation performance is approximately 130 s per epoch with 18 h and 17 min in total.

4 Results and Discussion

4.1 Classification Performance of the Modified ResNet50 Model. The performance of the modified ResNet50 model is visualized by both the histogram of prediction scores (see Fig. 6) and the confusion matrix heat map (see Fig. 7). The prediction scores of all test cases for left lung, right lung, and both lung obstructions are shown in Figs. 6(*a*)–6(*c*), respectively. The high score in each category indicates that the model has a high certainty, and the case will be classified based on the highest prediction score's class. As shown in Figs. 6(*a*)–6(*c*), most of the test cases have the highest prediction scores in the class with the same obstruction locations, which indicates the reliability of the prediction score system. Furthermore, as shown in Fig. 7 and Table 1, the testing dataset performance quantified by the average precision (AP) at a threshold of 0.5 is

- Left lung obstructed: AP = 89.27%,
- Right lung obstructed: AP = 93.89%, and
- Both lungs obstructed: AP = 98.43%.

The total accuracy converges to 95.1% after 20 epochs. Based on the testing result, the modified ResNet50 model is a reliable classifier to identify whether the obstruction is in the left lung, right lung, or both lungs with high sensitivity. The no obstruction case (i.e., normal airways) was studied, and the scores for both obstructions, left obstructions, and right obstruction are 0.3785, 0.3337, and 0.2878, respectively. Thus, the model is able to distinguish between obstruction cases and the healthy no-obstruction case.

4.2 Classification Performance of the YOLOv4 Model. To validate the modified ResNet50 model for classification and compare the sensitivity of AP to different CNN-based models, the YOLOv4 model was trained with two tests conducted (see Table 1). In the first test (i.e., test 1), to have a similar number of images for each class during training, we randomly selected 153, 153, and 153 images for left, right, and both lung obstructions, respectively. The values of precision (P), recall (R), and $F1$ *score* are listed in Table 1. Specifically, precision (P) represents the ability of the classifier to identify relevant data points that were classified as true and that were actually true. Recall (R) is

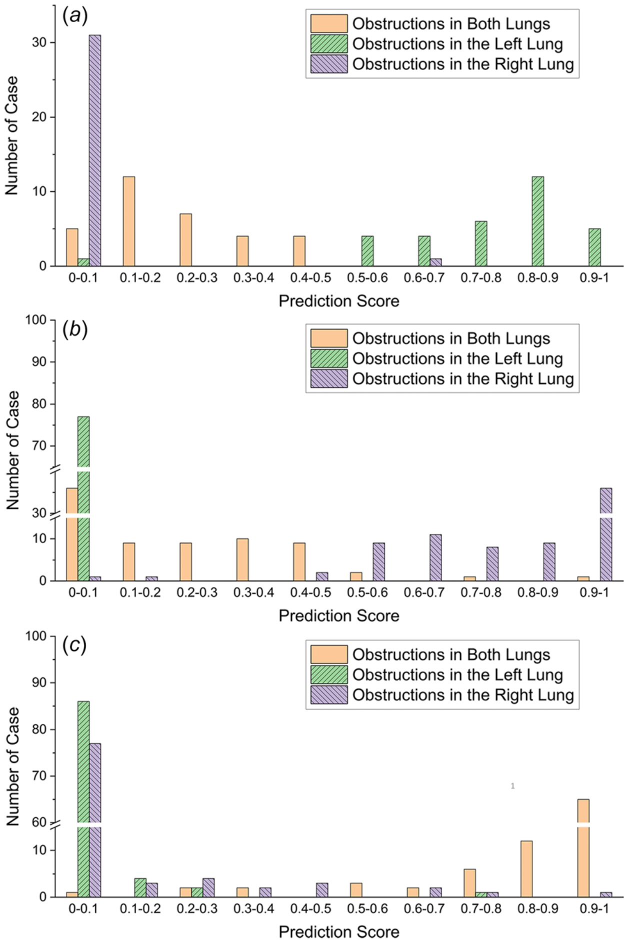

Fig. 6 Prediction scores for: (*a*) left lung obstructions, (*b*) right lung obstructions, and (*c*) both lungs obstructions

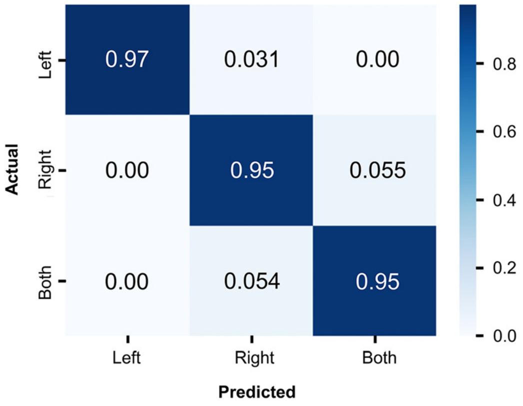

Fig. 7 Confusion matrix heat map for prediction

described as the ability of the classifier to find all relevant data points. Maximizing P often comes at the expense of R and vice versa. The $F1$ score is considered as a parameter that can be more objectively reflecting both P and R. Determining the $F1$ score is useful in this assessment to ensure optimal precision (P) and recall scores (R) can be achieved. As shown in Table 1, the precision, recall, and F1 score are 0.93, 0.94, and 0.93 at a threshold of 0.5 for test 1, respectively. By checking the AP for each class, the recognition of right (AP = 96.78%) and both (AP = 93.85%) lungs obstructions were not as good as recognition of the left lung obstruction (AP = 100%). Therefore, the second test (i.e., test 2) doubled the "right lung obstructed" images (from 153 to 378), and tripled the "both lung obstructed" images (from 153 to 459). APs slightly increased for the two classes (i.e., from 96.78% to 97.74% for right lung obstructions, and from 93.85% to 96.29% for both lung obstructions). Thus, the overall YOLOv4 model trained in test 2 is slightly better than test 1, with P increased from 0.93 to 0.96, R increased from 0.94 to 0.97, and $F1$ *score* increased from 0.93 to 0.96. The comparison of evaluation results between the modified ResNet50 and YOLOv4 models summarized in Table 1 shows that both models can be used as classifiers for the obstruction location identifications. Considering the computational costs shown in Sec. 3, ResNet50 is more efficient than YOLOv4.

4.3 Postprocessing Via Gradient-Weighted Class Activation Mapping Model and Hue-Value-Saturation. As shown in Fig. 8, the Grad-CAM model is combined with the modified ResNet50 model to output the heat map visualization of the important region. The HSV thresholding technique is applied to the heat map plot of the Grad-CAM model [15]. The HSV color space is a cylindrical coordinate representation of points in an RGB color model. It represents the human perception using Hue (the dominant color as perceived by an observer), Saturation (the amount of white light mixed with a Hue), and Value (the chromatic notion of intensity) [46]. The highlighted regions were detected by filtering out the color that suggests a low correlation with the obstructions. As shown in Fig. 9, the highlighted regions for cases within the same obstruction class (i.e., left lung, right lung, or both lungs) were blended with the same weight, for finding the most important regions to identify different obstructions. The brightness of the color shows the importance of the region for classification. It can be observed that the area of the bright red region for both lung obstructions is larger than that for left or right lung obstruction cases. It indicates that the determination of both lung obstructions requires more information.

4.4 Expiratory Airflow Velocity Contours: Flow Pattern Versus Obstructed Site. Although both the modified ResNet50 and YOLOv4 models can classify the obstruction locations well, more insights are still needed to be generated to answer the following two questions, i.e.,

(1) Is it necessary to employ CNN-based models for the obstruction location classification? In other words, if the expiratory velocity contours have significant pattern shifts between different obstruction classes that can be directly observed by the contour comparisons, then CNN-based

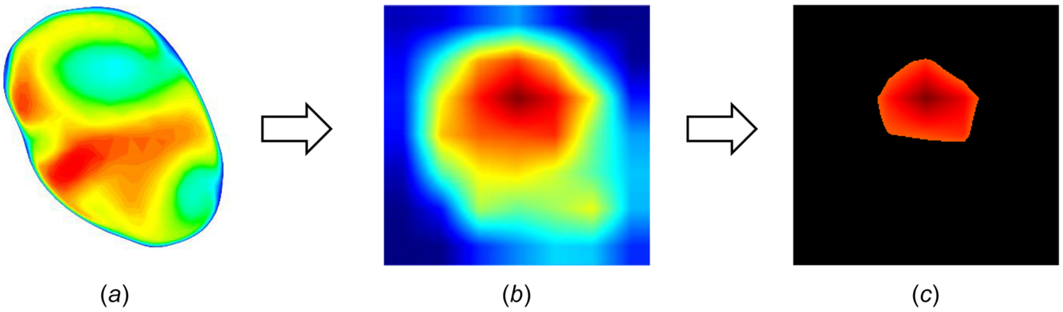
(*a*) (*b*) (*c*)

Fig. 8 HSV thresholding technique procedure

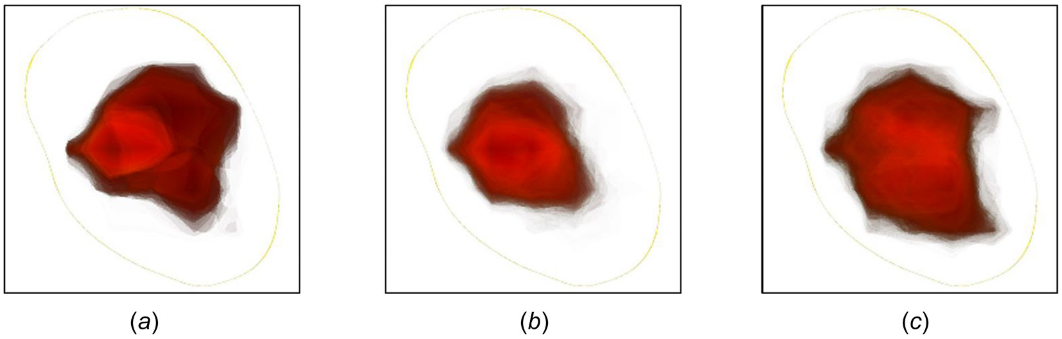
(*a*) (*b*) (*c*)

Fig. 9 Blended highlight regions of construction for: (*a*) left lung, (*b*) right lung, and (*c*) both lungs

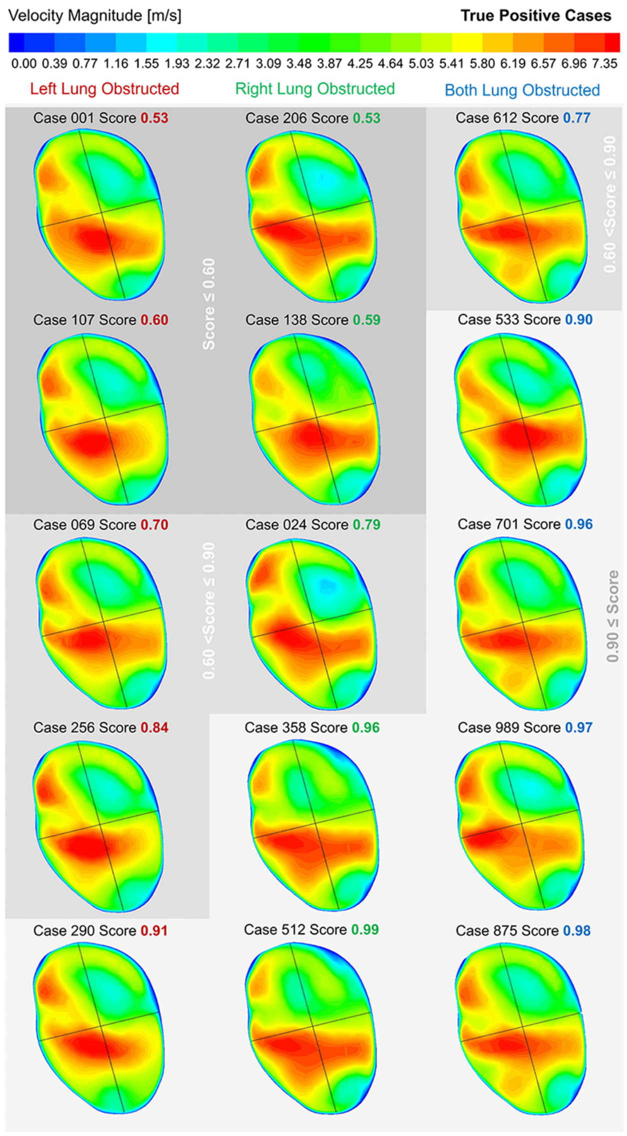

Fig. 10 Velocity contours ($x = 0.1$ m) of *true positive* cases with different obstruction sites

models are not necessary to employ for accurate classifications.

(2) What is the fundamental explanation for the high correlated regions shown in Fig. 9 used by the CNN-based model to classify the obstruction locations?

Therefore, to assess the airflow flow pattern shifts among the three categories of obstruction types (, , i.e., left lung, right lung, and both lung), velocity contours at the selected cross section ($x = 0.1$ m in Fig. 2) are visualized and compared. For each obstruction class, 5 true positive cases were randomly selected with the correct diagnosis using the two CNN-based models (see Fig. 10). In addition, those false positive cases were also selected and their velocity contours are visualized in Fig. 11. The case numbers and their prediction scores are listed in Table 2. To further quantify the velocity magnitude, velocity profiles along two lines (L_1 and L_2 shown in Fig. 2) are shown in Figs. 12 and 13. L_1^* and L_2^* are normalized lengths ranging from 0 to 1. Velocity contours for the other cases that were not listed in Table 2 can be found in Supplemental Material S1 on the ASME Digital Collection.

Figure 10 shows the velocity contours for randomly selected true positive cases with scores, providing direct visualizations of the contour differences among left obstructed, right obstructed, and both obstructed cases. Gray levels of the background indicate the ranges of the prediction scores for the contours. It can be found that no distinguished pattern shifts in velocity contours can be visually observed between cases with obstructions in different lungs. In addition, the quantitative comparisons of cases with high prediction scores (>0.90) shown in Figs. 12(*a*) and 13(*a*) can also support the above-mentioned observations. Specifically, no significant shifts in the velocity profiles shown in Figs. 12(*a*) and 13(*a*) can be identified among cases with different obstruction classes. Furthermore, it is also interesting to notice that although the prediction scores are close between case 989 (0.97) and case 875 (0.98) within the class of both lungs obstructed, their velocity profiles shown in Figs. 12(*a*) and 13(*a*) are significantly different from each other at $0.05 < L_1^* < 0.5$ and $0.05 < L_2^* < 0.45$. Figures 12(*b*)–12(*d*) and 13(*b*)–13(*d*) show that the velocity profiles are also not significantly different between cases with the same obstructed lungs but different prediction scores. Based on the comparisons mentioned above, it can be concluded that velocity contours and selected velocity profiles cannot show distinguished shifts between cases with different obstruction locations in small airways, indicating the necessity to involve CNN-based models to achieve accurate classifications.

Figure 11 visualizes the velocity contours of false positive cases. Compared with true positive cases shown in Fig. 10, some false positive cases show similar velocity distributions while others show noticeable differences. For example, the velocity contour of false positive case 027 (left obstructed, false positive as right obstructed) shows a similar high-velocity region near the left bottom corner similar to the true positive cases (i.e., cases 358 and 512) with right lung obstructed. In contrast, the contour of case 027 is more deviated from other true positive cases with left lung obstructed. However, case 310 (right obstructed, false positive both) has a velocity contour, which is highly different from the cases with right lung obstructed and cases with both lungs obstructed. Figures 12 and 13(*b*)–13(*d*) can also support such inconsistent observations between true and false positive cases. Specifically, Figs. 12 and 13(*b*)–13(*d*) compare the velocity profiles along lines L_1 and L_2 for cases grouped by their output classes based on the CNN-based results. For the cases identified as left obstructed or right obstructed, including both true and false positive scenarios (see Figs. 12–13(*b*) and 13(*c*)), the velocity profiles are similar to each other with minor differences. For the cases identified as both obstructed, including both true and false positive scenarios (see Figs. 12(*d*) and 13(*d*)), the velocity profiles are significantly different. Therefore, it can be concluded again that it is not possible to directly identify the obstruction locations in small airways from velocity contours and the velocity profiles without the assistance of CNN-based models.

4.5 Similarity Measurement of Velocity Contours Using Pearson Correlation.

Since Sec. 4.4 demonstrates that the airflow velocity pattern shifts cannot be identified directly from the contours, the difference between flow patterns among cases with different obstructed locations is quantified using the Pearson correlation coefficient [15]. For similarity analysis between two velocity contours, $N = 152$ equally spaced monitoring points were selected at the particular cross section $x = 0.1$ m (see Fig. 2) for the correlation coefficient calculation [47]. The correlation coefficient r can be calculated by

$$r = \frac{\sum_i \left(V_{A,i} - \bar{V}_A\right)\left(V_{B,i} - \bar{V}_B\right)}{\sqrt{\sum_i \left(V_{A,i} - \bar{V}_A\right)^2}\sqrt{\sum_i \left(V_{B,i} - \bar{V}_B\right)^2}} \quad i \in [0, N] \tag{3}$$

where $V_{A,i}$ and $V_{B,i}$ are the velocity magnitudes at particular monitoring point i in case A and case B. Specifically, the monitoring points will be numbered as an $1 \times N$ array. Indices i's for all

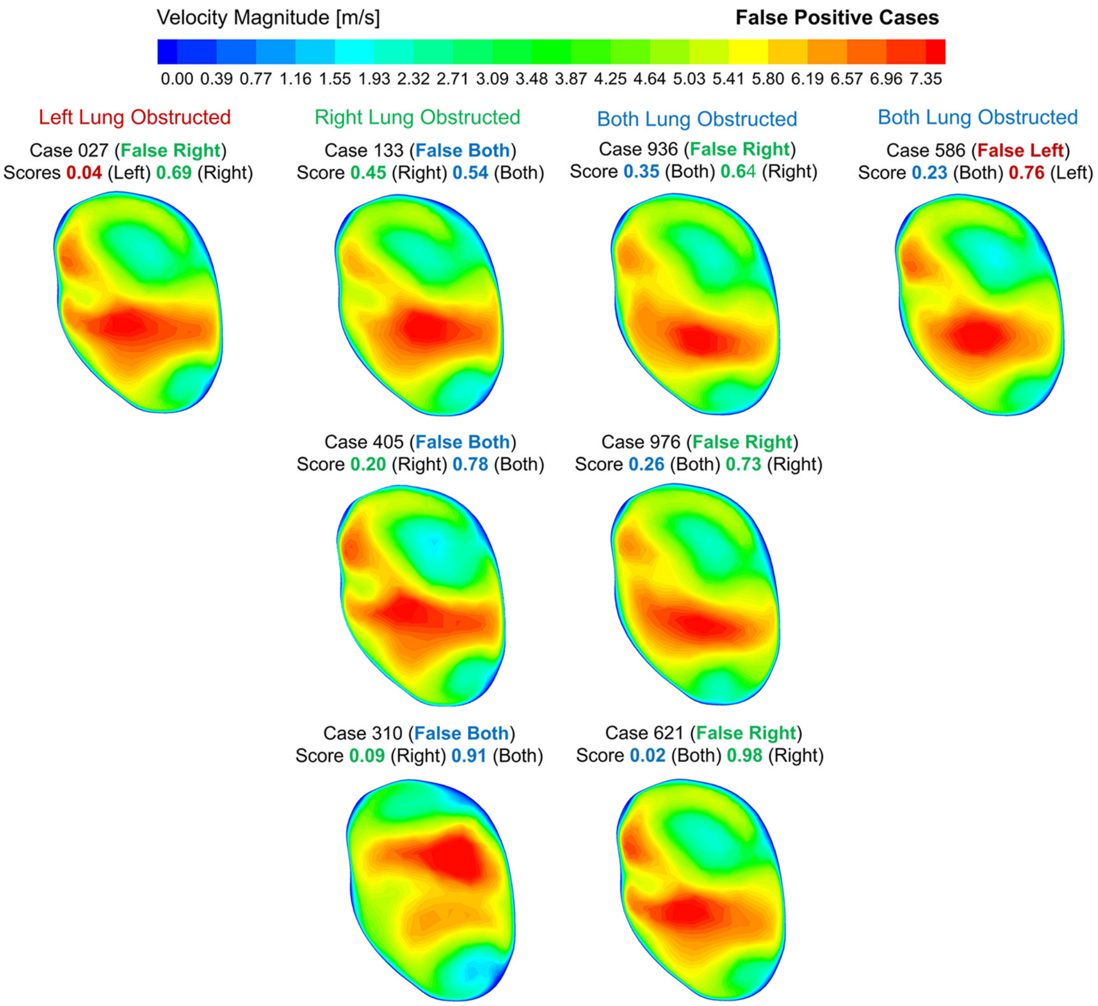

Fig. 11 Velocity contours ($x = 0.1$ m) of *false positive* cases with different obstruction sites

Table 2 Cases selected for the comparisons of airflow field shifts

True positive cases

Left lung obstructed		Right lung obstructed		Both lungs obstructed	
Case no.	Prediction score	Case no.	Prediction score	Case no.	prediction score
001	0.53	206	0.53	612	0.77
107	0.60	138	0.59	533	0.90
069	0.70	024	0.79	701	0.96
256	0.84	358	0.96	989	0.97
290	0.91	512	0.99	875	0.98

False positive cases

Left lung obstructed			Right lung obstructed			Both lungs obstructed		
Case no.	Prediction score		Case no.	Prediction score		Case no.	Prediction score	
027	0.04 (left)	0.69 (right)	310	0.09 (right)	0.91 (both)	586	0.23 (both)	0.77 (left)
			405	0.20 (right)	0.78 (both)	621	0.024 (both)	0.98 (right)
			017	0.44 (right)	0.56 (both)	976	0.26 (both)	0.73 (right)
			133	0.45 (right)	0.54 (both)	544	0.32 (both)	0.68 (right)
						936	0.35 (both)	0.64 (right)

monitoring points are shown in Fig. 2. $\bar{V}_A$ and $\bar{V}_B$ denote the mean velocities of arrays $V_{A,i}$ and $V_{B,i}$, respectively. As also shown in Fig. 2, the monitoring points in the shaded region are also selected as the "filtered" points of interest, based on the regions that have a high correlation with the obstruction locations (see Fig. 9). The correlation coefficient r is also calculated on the "filtered" points, in order to evaluate the similarity without the influence of the monitoring points in the region of low correlation

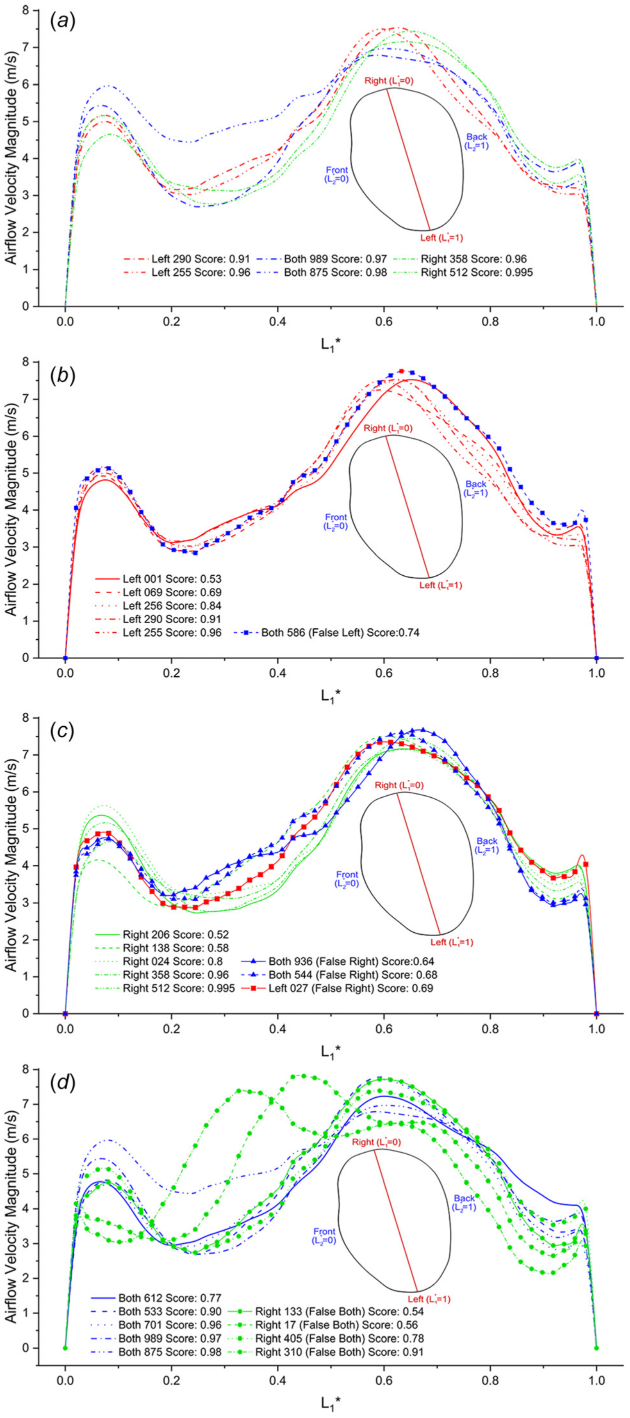

Fig. 12 Velocity profiles along line L_1: (*a*) selected cases with prediction scores higher than 0.9, (*b*) *true positive* cases versus *false positive* case (left obstructed), (*c*) true positive cases versus false positive cases (right obstructed), (*d*) true positive cases versus false positive cases (both obstructed)

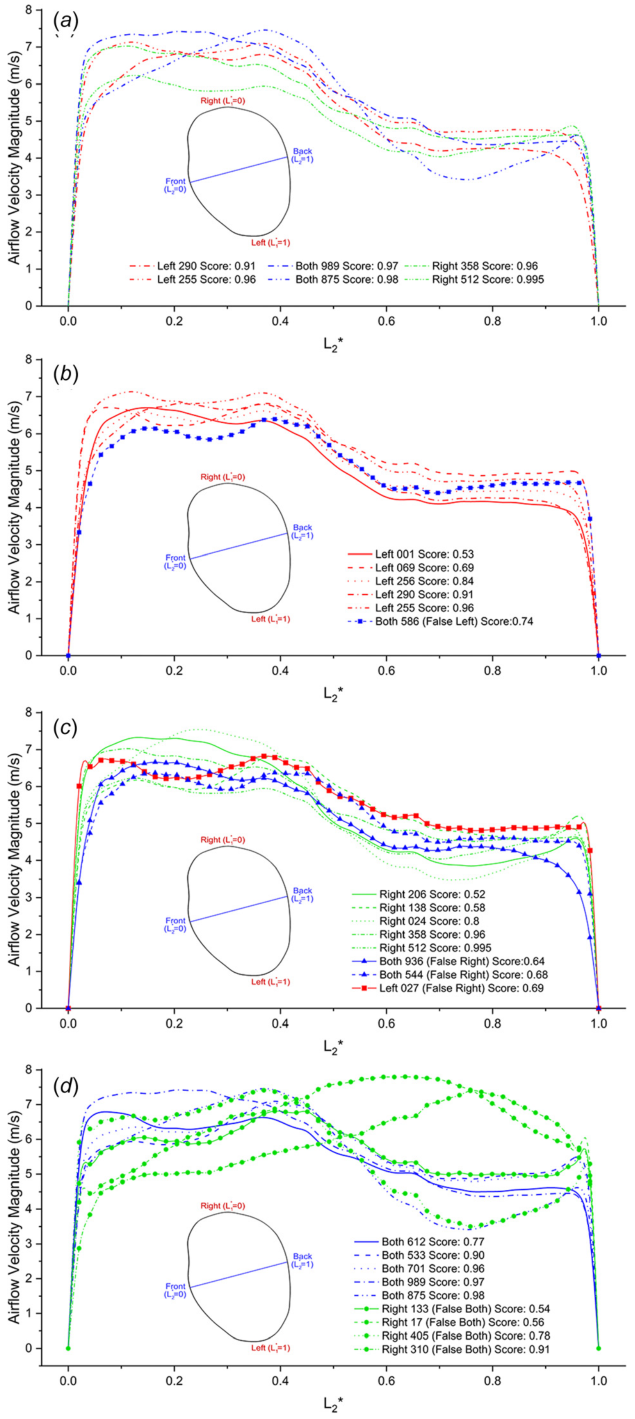

Fig. 13 Velocity profiles along line L_2: (*a*) selected cases with prediction scores higher than 0.9, (*b*) true positive cases versus false positive case (left obstructed), (*c*) true positive cases versus false positive cases (right obstructed), (*d*) true positive cases versus false positive cases (both obstructed)

(see Fig. 9). It is worth mentioning that high similarity is indicated if r is close to 1.0.

Tables 3–5 listed the r values for monitoring points in the unfiltered and filtered regions at the cross section ($x = 0.1$ m) among cases listed in Table 2. It can be observed from Tables 3–5 that the r values are close to or higher than 0.9 for "unfiltered" monitoring points, indicating the relatively high similarities between the velocity contours using the whole cross section area for cases with different obstruction locations. The exceptions, i.e., $r < 0.8$, are for the comparisons against the false positive case 310 and case 133, are due to the fact that their velocity contours (see Fig. 11) are significantly different from other cases (see Figs. 10 and 11). In contrast, the r values for the "filtered" monitoring points (see Fig. 11 and the shaded region in Fig. 2) are all less than 0.3, indicating the more significant shifts in velocity contours exist in the highly correlated regions shown in Figs. 9 and 11. The lower r values for the "filtered" region also show evidence of why it has a high correlation with the obstruction locations identified by Grad-CAM with HSV.

Table 3 Similarity measurements based on the Pearson correlation coefficient against expiratory velocity magnitude contours at the selected cross section ($x = 0.1$ m): Left obstructed cases versus right obstructed cases

Case no.	206 (right)	138 (right)	024 (right)	358 (right)	512 (right)
001 (left)	Unfiltered: 0.95 Filtered: 0.29	Unfiltered: 0.92 Filtered: 0.20	Unfiltered: 0.93 Filtered: 0.28	Unfiltered: 0.87 Filtered: 0.23	Unfiltered: 0.95 Filtered: 0.28
107 (left)	Unfiltered:0.95 Filtered: 0.28	Unfiltered: 0.92 Filtered:0.20	Unfiltered: 0.93 Filtered: 0.27	Unfiltered: 0.88 Filtered: 0.24	Unfiltered: 0.95 Filtered: 0.28
069 (left)	Unfiltered: 0.96 Filtered: 0.27	Unfiltered: 0.95 Filtered: 0.19	Unfiltered:0.93 Filtered: 0.25	Unfiltered: 0.92 Filtered: 0.23	Unfiltered: 0.95 Filtered: 0.26
256 (left)	Unfiltered: 0.96 Filtered: 0.29	Unfiltered: 0.92 Filtered: 0.21	Unfiltered: 0.94 Filtered: 0.28	Unfiltered: 0.88 Filtered: 0.24	Unfiltered: 0.95 Filtered: 0.28
290 (left)	Unfiltered: 0.92 Filtered: 0.29	Unfiltered: 0.89 Filtered: 0.21	Unfiltered: 0.91 Filtered: 0.28	Unfiltered: 0.83 Filtered: 0.23	Unfiltered: 0.91 Filtered: 0.28
027 (left) (false right)	Unfiltered: 0.97 Filtered: 0.27	Unfiltered: 0.96 Filtered: 0.20	Unfiltered: 0.94 Filtered: 0.25	Unfiltered: 0.93 Filtered: 0.24	Unfiltered: 0.97 Filtered: 0.27

Table 4 Similarity measurements based on the Pearson correlation coefficient against expiratory velocity magnitude contours at the selected cross section ($x = 0.1$ m): both obstructed cases versus left obstructed cases

Case no.	001 (left)	107 (left)	069 (left)	256 (left)	290 (left)
612 (both)	Unfiltered: 0.93 Filtered: 0.24	Unfiltered: 0.95 Filtered: 0.24	Unfiltered: 0.99 Filtered: 0.24	Unfiltered: 0.96 Filtered: 0.25	Unfiltered: 0.91 Filtered:0.24
533 (both)	Unfiltered: 0.91 Filtered: 0.23	Unfiltered: 0.93 Filtered: 0.24	Unfiltered: 0.97 Filtered: 0.23	Unfiltered: 0.94 Filtered: 0.25	Unfiltered: 0.90 Filtered: 0.24
701 (both)	Unfiltered: 0.93 Filtered: 0.23	Unfiltered: 0.94 Filtered: 0.23	Unfiltered: 0.98 Filtered: 0.23	Unfiltered: 0.95 Filtered: 0.24	Unfiltered: 0.93 Filtered: 0.24
989 (both)	Unfiltered: 0.93 Filtered: 0.26	Unfiltered: 0.94 Filtered: 0.26	Unfiltered: 0.97 Filtered: 0.25	Unfiltered: 0.95 Filtered: 0.27	Unfiltered: 0.91 Filtered: 0.26
875 (both)	Unfiltered: 0.89 Filtered: 0.22	Unfiltered: 0.89 Filtered: 0.21	Unfiltered: 0.89 Filtered: 0.19	Unfiltered: 0.90 Filtered: 0.22	Unfiltered: 0.88 Filtered: 0.23
586 (both) (false left)	Unfiltered: 0.98 Filtered: 0.26	Unfiltered: 0.98 Filtered: 0.26	Unfiltered: 0.96 Filtered: 0.24	Unfiltered: 0.97 Filtered: 0.26	Unfiltered: 0.94 Filtered: 0.26

5 Conclusions

The prototype of the novel, effective, and noninvasive tool for early diagnosis of deeper airway obstructions has been developed using CFD and two CNN-based models. The important regions have been determined by Grad-CAM and HSV thresholding techniques, and confirmed by the Pearson correlation coefficient calculations between CFD velocity contours. The reason for the falsely classified cases was analyzed based on the comparisons of fundamental airflow dynamics in the intrathoracic region. Key conclusions are summarized as follows:

(1) The two CNN-based models (i.e., modified ResNet50 and YOLOv4) can detect small airway obstruction locations based on measurable expiratory airflow patterns in the intrathoracic region well with all evaluation scores higher than 93%, including precision, recall, F1 score, and average precisions. YOLOv4 is slightly better in classification performance than the modified ResNet50 but requires a higher computational cost. Furthermore, the results of the two CNN-based models validate each other very well. The bagging or boosting ensemble method can be applied to achieve better overall prediction accuracy.

(2) The comparisons of expiratory velocity contours show minor flow field pattern shifts with the variations of obstruction sites, and demonstrate the necessity of employing CNN algorithms for the effective diagnosis of obstructions. In addition, the Pearson correlation coefficients show much lower similarities of the velocity contours in the highly correlated region identified by CNN-based models than the velocity contours of the whole cross section, which explains why the Grad-CAM and HSV technique relies more on the high correlated regions to identify the obstruction locations.

This prototype of the diagnostic algorithms paves the way for the development of noninvasive and effective diagnostic tools with classification algorithms to effectively diagnose COPD at an early stage and provide high-resolution information for precise treatment (i.e., targeted drug delivery to the identified obstruction sites) with better therapeutic outcomes. No CFD knowledge is needed for users (i.e., physicians) to use the classification algorithm, which increases the transformative impact of the CNN-based models for clinical practice.

6 Limitations of this Study

This study developed a prototype of the diagnostic algorithm to identify lung obstruction locations via the expiratory airflow distributions in the trachea, integrating CFD and CNN. Limitations of the study are listed as follows:

(1) Only one subject-specific TB tree configuration was employed in the CFD simulation for the preparation of

Table 5 Similarity measurements based on the Pearson correlation coefficient against expiratory velocity magnitude contours at the selected cross section ($x = 0.1$ m): right obstructed cases versus both obstructed cases

Case no.	206 (right)	138 (right)	024 (right)	358 (right)	512 (right)	310 (right) (false both)	405 (right) (false both)	017 (right) (false both)	133 (right) (false both)
612 (both)	Unfiltered: 0.96 Filtered: 0.27	Unfiltered: 0.93 Filtered: 0.19	Unfiltered: 0.93 Filtered: 0.25	Unfiltered: 0.91 Filtered: 0.23	Unfiltered: 0.94 Filtered: 0.26	Unfiltered: 0.49 Filtered: -0.09	Unfiltered: 0.97 Filtered: 0.26	Unfiltered: 0.67 Filtered: -0.0024	Unfiltered: 0.3 Filtered: 0.22
533 (both)	Unfiltered: 0.92 Filtered: 0.26	Unfiltered: 0.97 Filtered: 0.20	Unfiltered: 0.91 Filtered: 0.24	Unfiltered: 0.92 Filtered: 0.22	Unfiltered: 0.94 Filtered: 0.26	Unfiltered: 0.57 Filtered: -0.07	Unfiltered: 0.96 Filtered: 0.26	Unfiltered: 0.76 Filtered: 0.027	Unfiltered: 0.99 Filtered: 0.23
701 (both)	Unfiltered: 0.92 Filtered: 0.25	Unfiltered: 0.97 Filtered: 0.19	Unfiltered: 0.91 Filtered: 0.24	Unfiltered: 0.90 Filtered: 0.21	Unfiltered: 0.93 Filtered: 0.25	Unfiltered: 0.59 Filtered: -0.08	Unfiltered: 0.95 Filtered: 0.25	Unfiltered: 0.76 Filtered:0.017	Unfiltered: 0.99 Filtered: 0.22
989 (both)	Unfiltered: 0.98 Filtered: 0.30	Unfiltered: 0.89 Filtered: 0.20	Unfiltered: 0.96 Filtered: 0.28	Unfiltered: 0.89 Filtered: 0.25	Unfiltered: 0.93 Filtered: 0.28	Unfiltered: 0.38 Filtered: -0.11	Unfiltered: 0.97 Filtered: 0.28	Unfiltered: 0.59 Filtered: -0.002	Unfiltered: 0.90 Filtered: 0.22
875 (both)	Unfiltered: 0.91 Filtered: 0.23	Unfiltered: 0.87 Filtered: 0.17	Unfiltered: 0.96 Filtered: 0.25	Unfiltered: 0.81 Filtered: 0.17	Unfiltered: 0.86 Filtered: 0.21	Unfiltered: 0.43 Filtered: -0.09	Unfiltered: 0.93 Filtered: 0.24	Unfiltered: 0.59 Filtered: -0.02	Unfiltered: 0.87 Filtered: 0.18
621 (both) (False right)	Unfiltered: 0.97 Filtered: 0.28	Unfiltered: 0.94 Filtered: 0.20	Unfiltered: 0.94 Filtered: 0.26	Unfiltered: 0.24 Filtered: 0.91	Unfiltered: 0.96 Filtered: 0.28	Unfiltered: 0.46 Filtered: -0.09	Unfiltered: 0.97 Filtered: 0.27	Unfiltered: 0.66 Filtered: 0.001	Unfiltered: 0.96 Filtered: 0.23
976 (both) (False right)	Unfiltered: 0.90 Filtered: 0.27	Unfiltered: 0.90 Filtered: 0.19	Unfiltered: 0.89 Filtered: 0.26	Unfiltered: 0.82 Filtered: 0.22	Unfiltered: 0.91 Filtered: 0.26	Unfiltered: 0.47 Filtered: -0.09	Unfiltered: 0.90 Filtered: 0.25	Unfiltered: 0.62 Filtered: -0.02	Unfiltered: 0.91 Filtered: 0.21
544 (both) (False right)	Unfiltered: 0.92 Filtered: 0.25	Unfiltered: 0.95 Filtered: 0.19	Unfiltered: 0.90 Filtered: 0.24	Unfiltered: 0.89 Filtered: 0.21	Unfiltered: 0.94 Filtered: 0.25	Unfiltered: 0.53 Filtered: -0.08	Unfiltered: 0.94 Filtered: 0.24	Unfiltered: 0.69 Filtered: -0.005	Unfiltered: 0.96 Filtered: 0.21
936 (both) (False right)	Unfiltered: 0.91 Filtered: 0.27	Unfiltered: 0.91 Filtered: 0.19	Unfiltered: 0.90 Filtered: 0.26	Unfiltered: 0.84 Filtered: 0.22	Unfiltered: 0.93 Filtered: 0.26	Unfiltered: 0.46 Filtered:-0.096	Unfiltered: 0.92 Filtered:0.25	Unfiltered: 0.62 Filtered: -0.02	Unfiltered: 0.92 Filtered: 0.20

training and test images, which did not consider the inter-subject variability effect and the influence of airway deformation kinematics.

(2) Obstructions were assumed to only appear in either the left lung, the right lung, or both lungs in the training and test images, which could be more specific to different lobes.

(3) The airway was assumed to be rigid, which neglected the effect of airway expansion and contraction in the real-world breathing process.

(4) The input image was produced by the CFD instead of real-world MRI images.

7 Future Work for Clinical Practice Transformation

To address the limitations of this study, and further develop a diagnosis algorithm that can be ready for clinical practice, future work includes:

(1) More subject-specific airway configurations with airway deformation kinematics [48] will be obtained and employed in the CFD simulations to prepare the training and test images with the effect of inter-subject variabilities, which will enhance the generalized predictability of the CNN algorithm.

(2) Lobe-specific obstruction diagnosis will be achieved by improving the training process of the two CNN-based models.

(3) Noises and missing parts could be added to mimic the real-world MRI images first, then replaced by hyperpolarized MRI images to further improve the accuracy and realism of the CNN algorithms.

The long-term goal is to provide physicians with a computationally efficient diagnosis algorithm, which can identify the obstruction locations in human lungs based on the pulmonary airflow velocity distributions that are measurable using hyperpolarized MRI [8–11].

Acknowledgment

This material is based upon work supported by the National Science Foundation under Grant No. CBET 2120688. The research was made possible by funding through the award for project number HR19-106, from the Oklahoma Center for the Advancement of Science and Technology (OCAST). The use of ANSYS software as part of the ANSYS-CBBL academic partnership is gratefully acknowledged. Some of the computing for this project was performed at the OSU High Performance Computing Center (Jesse Schafer, Head of Operations, OSU-HPCC) at Oklahoma State University, supported in part through the National Science Foundation grant OAC-1531128. The authors would like to thank Mrs. Pam Reynolds (Engineering Research Proposal Editor and Writer, College of Engineering, Architecture and Technology, Oklahoma State University) for constructive criticism of the paper.

Funding Data

- National Science Foundation (Grant No. CBET 2120688; Funder ID: 10.13039/100000001).

Data Availability Statement

The data that support the findings of this study are available from the corresponding author upon reasonable request.

References

[1] Hamilton, B. E., Hoyert, D. L., Martin, J. A., Strobino, D. M., and Guyer, B., 2013, "Annual Summary of Vital Statistics: 2010–2011," Pediatrics, **131**(3), pp. 548–558.

[2] Yi, H., Wang, Q., and Feng, Y., 2021, "Computational Analysis of Obstructive Disease and Cough Intensity Effects on the Mucus Transport and Clearance in an Idealized Upper Airway Model Using the Volume of Fluid Method," Phys. Fluids, **33**(2), p. 021903.

[3] Pramanik, S., Mohanto, S., Manne, R., Rajendran, R. R., Deepak, A., Edapully, S. J., Patil, T., and Katari, O., 2021, "Nanoparticle-Based Drug Delivery System: The Magic Bullet for the Treatment of Chronic Pulmonary Diseases," Mol. Pharm., **18**(10), pp. 3671–3718.

[4] Rajendran, R. R., and Banerjee, A., 2021, "Effect of Non-Newtonian Dynamics on the Clearance of Mucus From Bifurcating Lung Airway Models," ASME J. Biomech. Eng., **143**(2), p. 021011.

[5] Jindal, S. K., 2012, "COPD: The Unrecognized Epidemic in India," J. Assoc. Phys. India, **60**, pp. 14–6.

[6] Deepak, D., Prasad, A., Atwal, S. S., and Agarwal, K., 2017, "Recognition of Small Airways Obstruction in Asthma and COPD—The Road Less Travelled," J. Clin. Diagn. Res. JCDR, **11**(3), pp. TE01–TE05.

[7] Burgel, P.-R., Bergeron, A., De Blic, J., Bonniaud, P., Bourdin, A., Chanez, P., Chinet, T., Dalphin, J.-C., Devillier, P., Deschildre, A., Didier, A., Kambouchner, M., Knoop, C., Laurent, F., Nunes, H., Perez, T., Roche, N., Tillie-Leblond, I., and Dusser, D., 2013, "Small Airways Diseases, Excluding Asthma and COPD: An Overview," Eur. Respir. Rev., **22**(128), pp. 131–147.

[8] Roos, J. E., McAdams, H. P., Kaushik, S. S., and Driehuys, B., 2015, "Hyperpolarized Gas MR Imaging: Technique and Applications," Magn. Reson. Imaging Clin., **23**(2), pp. 217–229.

[9] Salerno, M., Altes, T. A., Brookeman, J. R., De Lange, E. E., and Mugler, J. P., III, 2001, "Dynamic Spiral MRI of Pulmonary Gas Flow Using Hyperpolarized 3He: Preliminary Studies in Healthy and Diseased Lungs," Magn. Reson. Med., **46**(4), pp. 667–677.

[10] Walkup, L. L., Thomen, R. P., Akinyi, T. G., Watters, E., Ruppert, K., Clancy, J. P., Woods, J. C., and Cleveland, Z. I., 2016, "Feasibility, Tolerability and Safety of Pediatric Hyperpolarized 129 Xe Magnetic Resonance Imaging in Healthy Volunteers and Children With Cystic Fibrosis," Pediatric Radiol., **46**(12), pp. 1651–1662.

[11] Walkup, L. L., and Woods, J. C., 2014, "Translational Applications of Hyperpolarized 3He and 129Xe," NMR Biomed., **27**(12), pp. 1429–1438.

[12] Sul, B., Oppito, Z., Jayasekera, S., Vanger, B., Zeller, A., Morris, M., Ruppert, K., Altes, T., Rakesh, V., Day, S., Robinson, R., Reifman, J., and Wallqvist, A., 2018, "Assessing Airflow Sensitivity to Healthy and Diseased Lung Conditions in a Computational Fluid Dynamics Model Validated In Vitro," ASME J. Biomech. Eng., **140**(5), p. 051009.

[13] He, K., Zhang, X., Ren, S., and Sun, J., 2016, "Deep Residual Learning for Image Recognition," Proceedings of the IEEE Conference on Computer Vision and Pattern Recognition, Las Vegas, NV, June 27–30.

[14] Bochkovskiy, A., Wang, C.-Y., and Liao, H.-Y. M., 2020, "Yolov4: Optimal Speed and Accuracy of Object Detection," arXiv Preprint arXiv:2004.10934.

[15] Daibo, M., 2017, "Toroidal Vector-Potential Transformer," Eleventh International Conference on Sensing Technology (ICST), IEEE, Sydney, New South Wales, Australia, Dec. 4–6.

[16] Li, Y., Wang, H., Dang, L. M., Nguyen, T. N., Han, D., Lee, A., Jang, I., and Moon, H., 2020, "A Deep Learning-Based Hybrid Framework for Object Detection and Recognition in Autonomous Driving," IEEE Access, **8**, pp. 194228–194239.

[17] Sozzi, M., Cantalamessa, S., Cogato, A., Kayad, A., and Marinello, F., 2021, "Grape Yield Spatial Variability Assessment Using YOLOv4 Object Detection Algorithm," *Precision agriculture'21*, Wageningen Academic Publishers, Wageningen, The Netherlands, pp. 193–198.

[18] Kajabad, E. N., Begen, P., Nizomutdinov, B., and Ivanov, S., 2021, "YOLOv4 for Urban Object Detection: Case of Electronic Inventory in St. Petersburg," 2021 28th Conference of Open Innovations Association (FRUCT), IEEE, Moscow, Russia, Jan. 27-29.

[19] Cai, C., Nishimura, T., Hwang, J., Hu, X. M., and Kuroda, A., 2021, "Asbestos Detection With Fluorescence Microscopy Images and Deep Learning," Sensors, **21**(13), p. 4582.

[20] Chen, H., Yuan, X., Pei, Z., Li, M., and Li, J., 2019, "Triple-Classification of Respiratory Sounds Using Optimized S-Transform and Deep Residual Networks," IEEE Access, **7**, pp. 32845–32852.

[21] Young, H. M., Guo, F., Eddy, R. L., Maksym, G., and Parraga, G., 2018, "Oscillometry and Pulmonary MRI Measurements of Ventilation Heterogeneity in Obstructive Lung Disease: Relationship to Quality of Life and Disease Control," J. Appl. Physiol., **125**(1), pp. 73–85.

[22] Westcott, A., Capaldi, D. P., McCormack, D. G., Ward, A. D., Fenster, A., and Parraga, G., 2019, "Chronic Obstructive Pulmonary Disease: Thoracic CT Texture Analysis and Machine Learning to Predict Pulmonary Ventilation," Radiology, **293**(3), pp. 676–684.

[23] Labaki, W. W., and Han, M. K., 2018, "Artificial Intelligence and Chest Imaging. Will Deep Learning Make Us Smarter?," Am. J. Respir. Crit. Care Med., **197**(2), pp. 148–150.

[24] González, G., Ash, S. Y., Vegas-Sánchez-Ferrero, G., Onieva Onieva, J., Rahaghi, F. N., Ross, J. C., Díaz, A., San José Estépar, R., and Washko, G. R., 2018, "Disease Staging and Prognosis in Smokers Using Deep Learning in Chest Computed Tomography," Am. J. Respir. Crit. Care Med., **197**(2), pp. 193–203.

[25] Xi, J., Zhao, W., Yuan, J. E., Kim, J., Si, X., and Xu, X., 2015, "Detecting Lung Diseases From Exhaled Aerosols: Non-Invasive Lung Diagnosis Using Fractal Analysis and SVM Classification," PLoS One, **10**(9), p. e0139511.

[26] Xi, J., and Zhao, W., 2019, "Correlating Exhaled Aerosol Images to Small Airway Obstructive Diseases: A Study With Dynamic Mode Decomposition and Machine Learning," PLoS One, **14**(1), p. e0211413.

[27] Feng, Y., Zhao, J., Kleinstreuer, C., Wang, Q., Wang, J., Wu, D. H., and Lin, J., 2018, “An in Silico Inter-Subject Variability Study of Extra-Thoracic Morphology Effects on Inhaled Particle Transport and Deposition,” J. Aerosol Sci., **123**, pp. 185–207.

[28] Haghnegahdar, A., Zhao, J., Kozak, M., Williamson, P., and Feng, Y., 2019, “Development of a Hybrid CFD-PBPK Model to Predict the Transport and Translocation of Xenon Gas From a Subject-Specific Human Respiratory System to Systemic Regions,” Heliyon, **5**(4), p. e01461.

[29] Menter, F. R., Kuntz, M., and Langtry, R., 2003, “Ten Years of Industrial Experience With the SST Turbulence Model,” Turbul., Heat Mass Transfer, **4**(1), pp. 625–632.

[30] Feng, Y., Zhao, J., Chen, X., and Lin, J., 2017, “An in Silico Subject-Variability Study of Upper Airway Morphological Influence on the Airflow Regime in a Tracheobronchial Tree,” Bioengineering, **4**(4), p. 90.

[31] Zhang, Z., Kleinstreuer, C., and Hyun, S., 2012, “Size-Change and Deposition of Conventional and Composite Cigarette Smoke Particles During Inhalation in a Subject-Specific Airway Model,” J. Aerosol Sci., **46**, pp. 34–52.

[32] Ren, S., He, K., Girshick, R., and Sun, J., 2017, “Faster R-CNN: Towards Real-Time Object Detection With Region Proposal Networks,” IEEE Trans. Pattern Anal. Mach. Intell., **39**(6), pp. 1137–1149.

[33] Chen, Y., Li, W., Sakaridis, C., Dai, D., and Van Gool, L., 2018, “Domain Adaptive Faster R-CNN for Object Detection in the Wild,” Proceedings of the IEEE Conference on Computer Vision and Pattern Recognition, Salt Lake City, UT.

[34] Wu, M., Yue, H., Wang, J., Huang, Y., Liu, M., Jiang, Y., Ke, C., and Zeng, C., 2020, “Object Detection Based on RGC Mask R-CNN,” IET Image Process., **14**(8), pp. 1502–1508.

[35] Sun, P., Zhang, R., Jiang, Y., Kong, T., Xu, C., Zhan, W., Tomizuka, M., Li, L., Yuan, Z., Wang, C., and Luo, P., 2021, “Sparse r-Cnn: End-to-End Object Detection With Learnable Proposals,” Proceedings of the IEEE/CVF Conference on Computer Vision and Pattern Recognition.

[36] Hochreiter, S., Bengio, Y., Frasconi, P., and Schmidhuber, J., 2001, “Gradient Flow in Recurrent Nets: The Difficulty of Learning Long-Term Dependencies,” *A Field Guide to Dynamical Recurrent Neural Networks*, IEEE Press, Hoboken, NJ.

[37] Goodfellow, I., Bengio, Y., and Courville, A., 2016, *Deep Learning*, MIT Press, Cambridge, MA.

[38] Deng, J., Dong, W., Socher, R., Li, L. J., Li, K., and Li, F., 2009, “Imagenet: A Large-Scale Hierarchical Image Database,” IEEE Conference on Computer Vision and Pattern Recognition, IEEE, Nashville, TN, June 20–25.

[39] Redmon, J., Divvala, S., Girshick, R., and Farhadi, A., 2016, “You Only Look Once: Unified, Real-Time Object Detection,” Proceedings of the IEEE Conference on Computer Vision and Pattern Recognition, Las Vegas, NV.

[40] Redmon, J., and Farhadi, A., 2017, “YOLO9000: Better, Faster, Stronger,” Proceedings of the IEEE Conference on Computer Vision and Pattern Recognition, Honolulu, HI.

[41] Redmon, J., and Farhadi, A., 2018, “Yolov3: An Incremental Improvement,” arXiv Preprint arXiv:1804.02767.

[42] Wang, C. Y., Liao, H. Y. M., Wu, Y. H., Chen, P. Y., Hsieh, J. W., and Yeh, I. H., 2020, “CSPNet: A New Backbone That Can Enhance Learning Capability of CNN,” Proceedings of the IEEE/CVF Conference on Computer Vision and Pattern Recognition Workshops, in.

[43] Liu, S., Qi, L., Qin, H., Shi, J., and Jia, J., 2018, “Path Aggregation Network for Instance Segmentation,” Proceedings of the IEEE Conference on Computer Vision and Pattern Recognition.

[44] Rajasegarar, S., Leckie, C., Palaniswami, M., and Bezdek, J. C., 2007, “Quarter Sphere Based Distributed Anomaly Detection in Wireless Sensor Networks,” IEEE International Conference on Communications, IEEE, Glasgow, UK, June 24–28.

[45] Shen, W. Z., Michelsen, J. A., and Sørensen, J. N., 2001, “Improved Rhie-Chow Interpolation for Unsteady Flow Computations,” AIAA J., **39**(12), pp. 2406–2409.

[46] Sural, S. G., Qian, S., and Pramanik, 2002, “Segmentation and Histogram Generation Using the HSV Color Space for Image Retrieval,” Proceedings of International Conference on Image Processing, IEEE, Rochester, NY.

[47] Dowdy, S., Wearden, S., and Chilko, D., 2011, *Statistics for Research*, Vol. 512, Wiley, Hoboken, NJ.

[48] Zhao, J., Feng, Y., Koshiyama, K., and Wu, H., 2021, “Prediction of Airway Deformation Effect on Pulmonary Air-Particle Dynamics: A Numerical Study,” Phys. Fluids, **33**(10), p. 101906.